A numerical study of Isogeometric Analysis for cavity flow and flow around a cylindrical obstacle

Babak S. Hosseini[1], Matthias Möller[2], and Stefan Turek[1]

[1]*TU Dortmund, Institute of Applied Mathematics (LS III), Vogelpothsweg 87, 44227 Dortmund, Germany*
[2]*Delft University of Technology, Department of Applied Mathematics, Mekelweg 4, 2628 CD Delft, The Netherlands*

Abstract

This paper presents our numerical results for the application of the Isogeometric Analysis (IGA) to the velocity-pressure formulation of the steady state as well as the unsteady incompressible Navier-Stokes equations. For the approximation of the velocity and pressure fields, LBB compatible spline spaces are used which can be regarded as generalizations of Taylor-Hood pairs of finite element spaces. The single-step θ-scheme is used for the discretization in time. The lid-driven cavity flow in addition to its regularized version and flow around cylinder are considered in two dimensions as model problems in order to investigate the numerical properties of the scheme with respect to accuracy.

Keywords:
Isogeometric Analysis; Isogeometric finite elements; B-splines; NURBS; Fluid mechanics, Navier-Stokes equations, lid-driven cavity flow, flow around cylinder.

1 Introduction

The Isogeometric analysis technique, developed by Hughes et al. [5], is a powerful numerical technique aiming to bridge the gap between the worlds of computer-aided engineering (CAE) and computer-aided design (CAD). It unites the benefits of Finite Element Analysis (FEA) with the ability of an exact representation of complex computational domains via an elegant mathematical description in form of uni-, bi- or trivariate non-uniform rational splines. Non-Uniform Rational B-splines (NURBS) are the de facto industry standard when it comes to modeling complex geometries, while FEA is a numerical approximation technique, that is widely used in computational mechanics.

NURBS and FEA utilize basis functions for the representation of geometry and approximation of field variables, respectively. In order to close the gap between the two technologies, Isogeometric Analysis adopts the spline geometry as the computational domain and utilizes its basis functions to construct both trial and test spaces in the discrete variational formulation of differential problems. The usage of these functions allows the construction of approximation spaces exhibiting higher regularity ($\mathcal{C}^{\geq 0}$) which - depending on the problem to be solved - may be beneficial compared to standard finite element spaces. In fact, primal variational formulations of high order partial differential equations (PDEs) such as Navier-Stokes-Korteweg (3-rd order spatial derivatives) or Cahn-Hilliard (4-th order spatial derivatives) require piecewise smooth and globally $\mathcal{C}^1$ continuous basis functions. The number of finite elements possessing $\mathcal{C}^1$ continuity and being applicable to complex geometries is already very limited in two dimensions [9, 10]. The Isogeometric Analysis technology features a unique combination of attributes, namely, superior accuracy on degree of freedom basis, robustness, two- and three-dimensional geometric flexibility, compact support, and the possibility for $\mathcal{C}^{\geq 0}$ continuity [5].

This article is all about the application and assessment of the Isogeometric Analysis approach to fluid flows with respect to well known benchmark problems. We present our numerical results for the lid-driven cavity flow problem (including its regularized version) using different spline approximation spaces and compare them to reference results from literature. Despite the fact that investigations of lid-driven cavity type model problems do not necessarily reflect the current spirit of time, they are nonetheless a natural first choice when its comes to assessing the properties of a numerical scheme.
Subsequent to lid-driven cavity, we eventually proceed to present and compare approximated physical quantities such as the drag and lift coefficients obtained for the flow around cylinder benchmark, whereby a multi-patch discretization approach is adopted. For the scenarios addressed, Isogeometric Analysis is applied on the steady-state as well as transient incompressible Navier-Stokes equations. For the equations under consideration are of nonlinear nature, we decided to provide a rather detailed insight concerning their treatment. The efficient solution of the discretized system of equations using iterative solution techniques such as, e.g., multigrid is not addressed in this paper. Preliminary research results are underway and will be presented in a forthcoming publication. In this numerical study, all systems of equations have been solved by a direct solver.

The outline of this paper is as follows. Section 2 is devoted to the introduction of the univariate and the multivariate (tensor product) B-spline and NURBS (non-uniform rational B-spline) basis functions, their related spaces and the NURBS geometrical map $\mathbf{F}$. This presentation is quite brief and notationally oriented. A more complete introduction to NURBS and Isogeometric Analysis can be found in [1, 5, 14]. Section 3 is dedicated to the presentation of the governing equations and their variational forms. In Sections 4 and 5, numerical results of Isogeometric Analysis of lid-driven cavity flow and flow around cylinder are presented and compared with reference results from literature.

2 Preliminaries

In order to fix the notation and for the sake of completeness, this section presents a brief overview of B-spline/NURBS basis functions and their corresponding spaces utilized in Isogeometric Analysis.
Isogeometric Analysis adopts spline (B-spline/NURBS, etc.) basis functions for analysis as well as for the description of the geometry (computational domain). Just like in FEA, a discrete approximation space - based on the span of the basis functions in charge - is constructed and eventually used in the framework of a Galerkin procedure for the numerical approximation of the solution of partial differential equations. Recalling reference ($\tilde{\Omega}$) and physical domains (Ω) in FEA, using B-splines/NURBS, one additional domain, the parametric spline space ($\hat{\Omega}$), needs to be considered as well (see Fig. 1). We follow this requirement and present an insight in the traits of spline based discrete approximation spaces in the sequel.

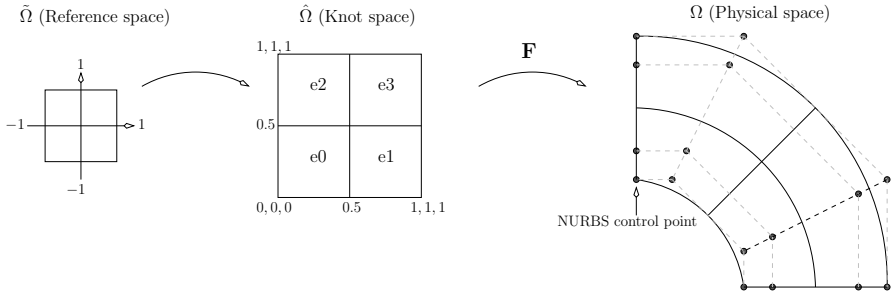

Figure 1: Domains involved in Isogeometric Analysis. Left: Reference domain used to evaluate integrals; Center: Exemplary parametric spline space with knot vectors $\Xi_u = \Xi_v := \{0, 0, 0, 0.5, 1, 1, 1\}$ defining four elements $(e0, \ldots, e3)$, two in each parametric direction. Right: Image of the knot space coordinates under the parameterization $\mathbf{F}$.

Given two positive integers p and n, we introduce the ordered knot vector

$$\Xi := \{0 = \xi_1, \xi_2, \ldots, \xi_m = 1\}, \tag{1}$$

whereby repetitions of the $m = n + p + 1$ knots ξ_i are allowed: $\xi_1 \leq \xi_2 \leq \cdots \leq \xi_m$. Note that in (1) the values of Ξ are normalized to the range $[0, 1]$ merely for the sake of clarity and not restricted in range otherwise. Besides, we assume that Ξ is an open knot vector, that is, the first and last knots have multiplicity $p + 1$:

$$\Xi = \{\underbrace{0, \ldots, 0}_{p+1}, \xi_{p+2}, \ldots, \xi_{m-p-1}, \underbrace{1, \ldots, 1}_{p+1}\}.$$

Let the (univariate) B-spline basis functions of degree p (order $p + 1$) be denoted by $B_{i,p}(\xi)$, for $i = 1, \ldots, n$. Then, the i-th B-spline basis function is a piecewise polynomial

function and it is recursively defined by the Cox-de Boor recursion formula:

$$
\begin{aligned}
B_{i,0}(\xi) &= \begin{cases} 1, & \text{if } \xi_i \leq \xi < \xi_{i+1} \\ 0, & \text{otherwise} \end{cases} \\
B_{i,p}(\xi) &= \frac{\xi - \xi_i}{\xi_{i+p} - \xi_i} B_{i,p-1}(\xi) + \frac{\xi_{i+p+1} - \xi}{\xi_{i+p+1} - \xi_{i+1}} B_{i+1,p-1}(\xi), \quad p > 0.
\end{aligned}
\tag{2}
$$

At knot ξ_i the basis functions have $\alpha := p - r_i$ continuous derivatives, where r_i denotes the multiplicity of knot ξ_i. The quantity α is bounded from below and above by $-1 \leq \alpha \leq p - 1$. Thus, the maximum multiplicity allowed is $r_i = p + 1$, rendering the basis functions at ξ_i discontinuous as it is the case at the boundaries of the interval.

Each basis function $B_{i,p}$ is non-negative over its support (ξ_i, ξ_{i+p+1}). The interval (ξ_i, ξ_{i+1}) is referred to as a knot span or element in IGA speak. Moreover, the B-spline basis functions are linearly independent and constitute a partition of unity, that is, $\sum_{i=1}^{n} B_{i,p}(\xi) = 1$ for all $\xi \in [0, 1]$. Figure 2 illustrates the basis functions of degree 2 of an exemplary knot vector exhibiting different levels of continuity. Due to the recursive definition (2), the

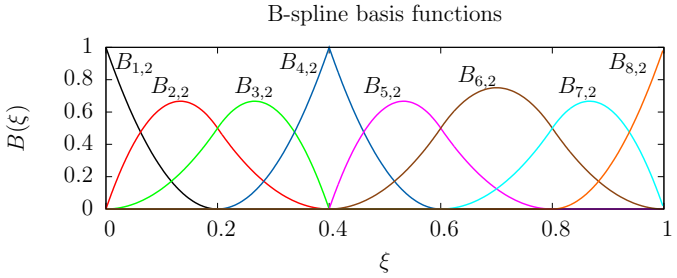

Figure 2: Plot of B-spline basis functions of degree 2 corresponding to the open knot vector $\Xi := \{0, 0, 0, 0.2, 0.4, 0.4, 0.6, 0.8, 1, 1, 1\}$. Due to the open knot vector trait, the first and last basis functions are interpolatory, that is, they take the value 1 at the first and last knot. At an interior knot ξ_i the continuity is $\mathcal{C}^{p-r_i}$ with r_i denoting the multiplicity of knot ξ_i. Due to the multiplicity $r_5 = 2$ of knot $\xi_5 = 0.4$, the continuity of the basis functions at this parametric point is $\mathcal{C}^{p-2} = \mathcal{C}^0$, while at the other interior knots the continuity is $\mathcal{C}^{p-1} = \mathcal{C}^1$.

derivative of the i-th B-spline basis function is given by

$$
B'_{i,p}(\xi) = \frac{p}{\xi_{i+p} - \xi_i} B_{i,p-1}(\xi) - \frac{p}{\xi_{i+p+1} - \xi_{i+1}} B_{i+1,p-1}(\xi) \tag{3}
$$

which is a combination of lower order B-spline functions. The generalization to higher derivatives is straightforward by simply differentiating each side of the above relation. Univariate rational B-spline basis functions are obtained by augmenting the set of B-spline basis functions with weights w_i and defining:

$$
R_{i,p}(\xi) = \frac{B_{i,p}(\xi) w_i}{W(\xi)}, \qquad W(\xi) = \sum_{j=1}^{n} B_{j,p}(\xi) w_j. \tag{4}
$$

Its derivative is obtained by simply applying the quotient rule. By setting all weighting coefficients equal to one it follows that B-splines are just a special case of NURBS.

The space of B-splines of degree p and regularity α determined by the knot vector Ξ is spanned by the basis functions $B_{i,p}$ and will be denoted by

$$\mathcal{S}_\alpha^p \equiv \mathcal{S}_\alpha^p(\Xi, p) := \text{span}\{B_{i,p}\}_{i=1}^n. \tag{5}$$

Analogously, we define the space spanned by rational B-spline basis functions as

$$\mathcal{N}_\alpha^p \equiv \mathcal{N}_\alpha^p(\Xi, p, w) := \text{span}\{R_{i,p}\}_{i=1}^n. \tag{6}$$

The definition of univariate B-spline spaces can readily be extended to higher dimensions. To this end, we consider d knot vectors Ξ_β, $1 \leq \beta \leq d$ and an open parametric domain $(0,1)^d \in \mathbb{R}^d$. The knot vectors Ξ_β partition the parametric domain $(0,1)^d$ into d-dimensional open knot spans, or elements, and thus yield a mesh $\mathcal{Q}$ being defined as

$$\mathcal{Q} \equiv \mathcal{Q}(\Xi_1, \ldots, \Xi_d) := \{Q = \otimes_{\beta=1}^d (\xi_{i,\beta}, \xi_{i+1,\beta}) \mid Q \neq \emptyset,\ 1 \leq i \leq m_\beta\} \tag{7}$$

For an element $Q \in \mathcal{Q}$, we set $h_Q = \text{diam}(Q)$, and define the global mesh size $h = \max\{h_Q, Q \in \mathcal{Q}\}$. We define the tensor product B-spline and NURBS basis functions as

$$B_{i_1,\ldots,i_d} := B_{i_1,1} \otimes \cdots \otimes B_{i_d,d}, \quad i_1 = 1, \ldots, n_1, \quad i_d = 1, \ldots, n_d \tag{8}$$

and

$$R_{i_1,\ldots,i_d} := R_{i_1,1} \otimes \cdots \otimes R_{i_d,d}, \quad i_1 = 1, \ldots, n_1, \quad i_d = 1, \ldots, n_d, \tag{9}$$

respectively. Then, the tensor product B-spline and NURBS spaces, spanned by the respective basis functions, are defined as

$$\mathcal{S}_{\alpha_1,\ldots,\alpha_d}^{p_1,\ldots,p_d} \equiv \mathcal{S}_{\alpha_1,\ldots,\alpha_d}^{p_1,\ldots,p_d}(\mathcal{Q}) := \mathcal{S}_{\alpha_1}^{p_1} \otimes \cdots \otimes \mathcal{S}_{\alpha_d}^{p_d} = \text{span}\{B_{i_1\ldots i_d}\}_{i_1=1,\ldots,i_d=1}^{n_1,\ldots,n_d} \tag{10}$$

and

$$\mathcal{N}_{\alpha_1,\ldots,\alpha_d}^{p_1,\ldots,p_d} \equiv \mathcal{N}_{\alpha_1,\ldots,\alpha_d}^{p_1,\ldots,p_d}(\mathcal{Q}) := \mathcal{N}_{\alpha_1}^{p_1} \otimes \cdots \otimes \mathcal{N}_{\alpha_d}^{p_d} = \text{span}\{R_{i_1\ldots i_d}\}_{i_1=1,\ldots,i_d=1}^{n_1,\ldots,n_d}, \tag{11}$$

respectively. The space $\mathcal{S}_{\alpha_1,\ldots,\alpha_d}^{p_1,\ldots,p_d}$ is fully characterized by the triangulation $\mathcal{Q}$, the degrees $p_1, \ldots, p_d$ of basis functions and their continuities $\alpha_1, \ldots, \alpha_d$. The minimum regularity/continuity of the space is $\alpha := \min\{\alpha_i, i \in (1,d)\}$.
For a representation of the elements in the physical domain Ω, the triangulation $\mathcal{Q}$ is mapped to the physical space via a NURBS geometrical map $\mathbf{F} : \hat{\Omega} \to \Omega$

$$\mathbf{F} = \sum_{i_1=1}^{n_1} \cdots \sum_{i_d=1}^{n_d} R_{i_1}(\xi_{i_1}) \ldots R_{i_d}(\xi_{i_d}) \mathbf{P}_{i_1,\ldots,i_d} \tag{12}$$

yielding a triangulation $\mathcal{K}$, with

$$\mathcal{K} = \mathbf{F}(Q) := \{\mathbf{F}(\boldsymbol{\xi}) | \boldsymbol{\xi} \in Q\}. \tag{13}$$

With the definition of $\mathbf{F}$ at hand, the space $\mathcal{V}$ of NURBS basis functions on Ω, being the *push-forward* of the space $\mathcal{N}$, is defined as

$$\mathcal{V}^{p_1,\dots,p_d}_{\alpha_1,\dots,\alpha_d} \equiv \mathcal{V}^{p_1,\dots,p_d}_{\alpha_1,\dots,\alpha_d}(\mathcal{K}) := \mathcal{V}^{p_1}_{\alpha_1} \otimes \cdots \otimes \mathcal{V}^{p_d}_{\alpha_d} = \operatorname{span}\{R_{i_1\dots i_d} \circ \mathbf{F}^{-1}\}^{n_1,\dots,n_d}_{i_1=1,\dots,i_d=1} \tag{14}$$

In equation (12), $\mathbf{P}$, denotes a homogeneous NURBS control point uniquely addressed in the NURBS tensor product mesh by its indices.
We assume that the parameterization $\mathbf{F}$ is invertible, with smooth inverse, on each element $Q \in \mathcal{Q}$. A mesh stack $\{\mathcal{Q}_h\}_{h\leq h_0}$, with affiliated spaces, can be constructed via knot insertion as described, e.g., in [5] from an initial coarse mesh $\mathcal{Q}_0$, with the global mesh size h pointing to a refinement level index.

3 Governing equations

For stationary flow scenarios, the governing equations to be solved are the steady-state incompressible Navier-Stokes equations represented in strong form as

$$-\nu\nabla^2\boldsymbol{v} + (\boldsymbol{v}\cdot\nabla)\boldsymbol{v} + \nabla p = \boldsymbol{b} \quad \text{in } \Omega \tag{15a}$$
$$\nabla\cdot\boldsymbol{v} = 0 \quad \text{in } \Omega \tag{15b}$$
$$\boldsymbol{v} = \boldsymbol{v}_D \quad \text{on } \Gamma_D \tag{15c}$$
$$-p\boldsymbol{v} + \nu(\boldsymbol{n}\cdot\nabla)\boldsymbol{v} = \boldsymbol{t} \quad \text{on } \Gamma_N \tag{15d}$$

where $\Omega \subset \mathbb{R}^2$ is a bounded domain, ρ is the density, μ represents the dynamic viscosity, $\nu = \mu/\rho$ is the kinematic viscosity, $p = P/\rho$ denotes the normalized pressure, $\boldsymbol{b}$ is the body force term, $\boldsymbol{v}_D$ is the value of the velocity Dirichlet boundary conditions on the Dirichlet boundary Γ_D, $\boldsymbol{t}$ is the prescribed traction force on the Neumann boundary Γ_N and $\boldsymbol{n}$ is the outward unit normal vector on the boundary. The kinematic viscosity and the density of the fluid are assumed to be constant. The first and second equations in (15) are the momentum and continuity equations, respectively.

Their continuous mixed variational formulation reads:

$$\begin{cases} \text{Find } \boldsymbol{v} \in \boldsymbol{\mathcal{H}}^1_{\Gamma_D}(\Omega) \text{ and } p \in \mathcal{L}_2(\Omega)/\mathbb{R} \text{ such that,} & \\ a(\boldsymbol{w},\boldsymbol{v}) + c(\boldsymbol{v};\boldsymbol{w},\boldsymbol{v}) + b(\boldsymbol{w},p) = (\boldsymbol{w},\boldsymbol{b}) + (\boldsymbol{w},\boldsymbol{t})_{\Gamma_N} & \forall \boldsymbol{w} \in \boldsymbol{\mathcal{H}}^1_0(\Omega) \\ b(\boldsymbol{v},q) = 0 & \forall q \in \mathcal{L}_2(\Omega)/\mathbb{R}, \end{cases} \tag{16}$$

where $\mathcal{L}_2$ and $\boldsymbol{\mathcal{H}}^1$ are Sobolev spaces as defined in the finite element literature.

Replacement of the linear-, bilinear- and trilinear forms with their respective definitions

and application of integration by parts on (16), yields

$$\underbrace{\nu \int_\Omega \nabla \boldsymbol{w} \colon \nabla \boldsymbol{v} \, \mathrm{d}\Omega}_{a(\boldsymbol{w},\boldsymbol{v})} + \underbrace{\int_\Omega \boldsymbol{w} \cdot \boldsymbol{v} \cdot \nabla \boldsymbol{v} \, \mathrm{d}\Omega}_{c(\boldsymbol{v};\boldsymbol{w},\boldsymbol{v})} - \underbrace{\int_\Omega \nabla \cdot \boldsymbol{w} p \, \mathrm{d}\Omega}_{b(\boldsymbol{w},p)} - \underbrace{\int_\Omega q \nabla \cdot \boldsymbol{v} \, \mathrm{d}\Omega}_{b(\boldsymbol{v},q)} = \underbrace{\int_\Omega \boldsymbol{w} \cdot \boldsymbol{b} \, \mathrm{d}\Omega}_{(\boldsymbol{w},\boldsymbol{b})} + \underbrace{\int_{\partial\Omega} \nu \boldsymbol{w} \cdot (\nabla \boldsymbol{v} \cdot \boldsymbol{n}) \, \mathrm{d}\partial\Omega}_{(\boldsymbol{w},\boldsymbol{t})_{\Gamma_N}} - \int_{\partial\Omega} p \boldsymbol{w} \cdot \boldsymbol{n}, \mathrm{d}\partial\Omega \tag{17}$$

In addition to the stationary channel flow around a circular obstacle model problem, we also consider its unsteady counterpart (see Chap. 5). In the latter case, the unsteady incompressible Navier-Stokes equations, defined as

$$\frac{\partial \boldsymbol{v}}{\partial t} - \nu \nabla^2 \boldsymbol{v} + (\boldsymbol{v} \cdot \nabla)\boldsymbol{v} + \nabla p = \boldsymbol{b} \quad \text{in } \Omega \times]0, T[\tag{18a}$$

$$\nabla \cdot \boldsymbol{v} = 0 \quad \text{in } \Omega \times]0, T[\tag{18b}$$

$$\boldsymbol{v} = \boldsymbol{v}_D \quad \text{on } \Gamma_D \times]0, T[\tag{18c}$$

$$-p\boldsymbol{v} + \nu(\boldsymbol{n} \cdot \nabla)\boldsymbol{v} = \boldsymbol{t} \quad \text{on } \Gamma_N \times]0, T[\tag{18d}$$

$$\boldsymbol{v}(\boldsymbol{x}, 0) = \boldsymbol{v}_0(\boldsymbol{x}) \tag{18e}$$

are solved in time, whereby the initial condition is required to satisfy $\nabla \cdot \boldsymbol{v}_0 = 0$. The corresponding variational problem reads: Find $\boldsymbol{v}(\boldsymbol{x}, t) \in \boldsymbol{\mathcal{H}}^1_{\Gamma_D}(\Omega) \times]0, T[$ and $p(\boldsymbol{x}, t) \in \mathcal{L}_2(\Omega) \times]0, T[$, such that for all $(\boldsymbol{w}, q) \in \boldsymbol{\mathcal{H}}^1_{\Gamma_0}(\Omega) \times \mathcal{L}_2(\Omega)/\mathbb{R}$ it holds

$$\begin{cases} (\boldsymbol{w}, \boldsymbol{v}_t) + a(\boldsymbol{w}, \boldsymbol{v}) + c(\boldsymbol{v}; \boldsymbol{w}, \boldsymbol{v}) + b(\boldsymbol{w}, p) = (\boldsymbol{w}, \boldsymbol{b}) + (\boldsymbol{w}, \boldsymbol{t})_{\Gamma_N} \\ b(\boldsymbol{v}, q) = 0 \end{cases} \tag{19}$$

Equations (15) and (18) both have a nonlinear advection term and require techniques for the treatment of nonlinear PDEs such as the Newton-Kantorovich method.

3.1 Treatment of Nonlinearity

We will apply Newton's method being basically a Taylor expansion followed by a linearization step. Willing to solve $f(x) = 0$ (with, e.g., $f : \mathbb{R} \to \mathbb{R}$) and having a good initial guess for a root, $x \approx x_{[i]}$, we apply a Taylor expansion of $f(x)$ around $x_{[i]}$ to obtain a power series approximation, given as:

$$f(x) = f(x_{[i]}) + f_x(x_{[i]})(x - x_{[i]}) + O((x - x_{[i]})^2) + ... \tag{20}$$

With a sufficiently good initial guess, one ignores the quadratic and other higher order terms and obtains the following update formula for x:

$$x_{[i+1]} = x_{[i]} - f(x_{[i]})/f_x(x_{[i]}) \tag{21}$$

Application of Newton's method on the incompressible steady-state Navier-Stokes equations, requires f to be a functional of the functions to be approximated (velocity and pressure) and f_x to be its Gâteaux differential. Expressing (17) in operator form

$$\mathcal{L}(\boldsymbol{v})\boldsymbol{v} = \boldsymbol{b}, \tag{22}$$

we let f be its (nonlinear) residual w.r.t the current state of the field variables

$$\mathcal{R}(\boldsymbol{v}^{n-1}) := \underbrace{(\mathcal{L}(\boldsymbol{v}^{n-1})\boldsymbol{v}^{n-1} - \boldsymbol{b})}_{\text{nonlinear residual}}. \tag{23}$$

It remains to find a representation for f_x.
The Gâteaux differential $dF(u;\psi)$ of F at $u \in U$ in the direction $\psi \in X$ - being the generalization of the concept of the directional derivative - is defined as

$$dF(u;\psi) = \lim_{\tau\to 0} \frac{F(u+\tau\psi) - F(u)}{\tau} = \frac{d}{d\tau} F(u+\tau\psi)\bigg|_{\tau=0}, \tag{24}$$

where X and Y are locally convex topological vector spaces, $U \subset X$ is open, $F : X \to Y$ and the limit exists. Aliasing $\tau\psi$ with $\bar{u}$, we express the above term as

$$F(u+\bar{u}) = F(u) + F'(u)\bar{u} + O(|\bar{u}|^2) \tag{25}$$

To derive the Jacobian of $\mathcal{L}$, let it be disassembled as $\mathcal{L} = \mathcal{L}_A \oplus \mathcal{L}_V \oplus \mathcal{L}_G \oplus \mathcal{L}_D$, with operators $\mathcal{L}_A = \boldsymbol{v}\cdot\nabla\boldsymbol{v}$, $\mathcal{L}_V = -\nu\nabla^2\boldsymbol{v}$, $\mathcal{L}_G = \nabla p$ and $\mathcal{L}_D = \nabla\cdot\boldsymbol{v}$. The Gâteaux differential of the nonlinear operator $\mathcal{L}_A$ with respect to the direction $\bar{\boldsymbol{v}}$, is derived as

$$\begin{aligned}
\mathcal{L}'_A(\boldsymbol{v})\bar{\boldsymbol{v}} &= \mathcal{L}_A(\boldsymbol{v}+\bar{\boldsymbol{v}}) - \mathcal{L}_A(\boldsymbol{v}) \\
&= [(\boldsymbol{v}+\bar{\boldsymbol{v}})\cdot\nabla(\boldsymbol{v}+\bar{\boldsymbol{v}})] - [\boldsymbol{v}\cdot\nabla\boldsymbol{v}] \\
&= [[\boldsymbol{v}\cdot\nabla(\boldsymbol{v}+\bar{\boldsymbol{v}})] + [\bar{\boldsymbol{v}}\cdot\nabla(\boldsymbol{v}+\bar{\boldsymbol{v}})]] - [\boldsymbol{v}\cdot\nabla\boldsymbol{v}] \\
&= [\boldsymbol{v}\cdot\nabla\boldsymbol{v} + \boldsymbol{v}\cdot\nabla\bar{\boldsymbol{v}} + \bar{\boldsymbol{v}}\cdot\nabla\boldsymbol{v} + \bar{\boldsymbol{v}}\cdot\nabla\bar{\boldsymbol{v}} - \boldsymbol{v}\cdot\nabla\boldsymbol{v}] \\
&= [\boldsymbol{v}\cdot\nabla\bar{\boldsymbol{v}} + \bar{\boldsymbol{v}}\cdot\nabla\boldsymbol{v} + \bar{\boldsymbol{v}}\cdot\nabla\bar{\boldsymbol{v}}]
\end{aligned} \tag{26}$$

The derivatives of the remaining operators $\mathcal{L}_V$, $\mathcal{L}_G$, and $\mathcal{L}_D$ can be obtained analogously. Their combination eventually yields

$$\mathcal{L}'(\boldsymbol{v})\bar{\boldsymbol{v}} := \begin{bmatrix} -\nu\nabla^2(\cdot) + (\cdot)\cdot\nabla\boldsymbol{v} + \boldsymbol{v}\cdot\nabla(\cdot) & \nabla(\cdot) \\ \nabla\cdot(\cdot) & 0 \end{bmatrix} \begin{bmatrix} \bar{\boldsymbol{v}} \\ \bar{p} \end{bmatrix} + \underbrace{\begin{bmatrix} \bar{\boldsymbol{v}}\cdot\nabla\bar{\boldsymbol{v}} \\ 0 \end{bmatrix}}_{O(|\bar{\boldsymbol{v}}|^2)\to 0} \tag{27}$$

Note that in (27), the symbol $(\cdot)$ denotes the basis functions of the respective perturbation functions $\bar{\boldsymbol{v}} = \sum_i \bar{\boldsymbol{v}}_i\varphi_i$ and $\bar{p} = \sum_i \bar{p}_i\psi_i$. Their coefficients $\bar{\boldsymbol{v}}_i$ and $\bar{p}_i$ are irrelevant in this context. With all required ingredients at hand, one nonlinear relaxation step is given by

$$\boldsymbol{v}^n = \boldsymbol{v}^{n-1} - \omega^{n-1}[\boldsymbol{J}(\boldsymbol{v}^{n-1})]^{-1} \underbrace{(\mathcal{L}(\boldsymbol{v}^{n-1})\boldsymbol{v}^{n-1} - \boldsymbol{b})}_{\text{nonlinear residual}}, \tag{28}$$

where, depending on the complexity to setup and evaluate the Jacobian matrix $\boldsymbol{J}$, one may decide to adopt $\mathcal{L}$ rather than $\mathcal{L}'$. The scalar quantity ω serves as damping parameter used for tuning and can, e.g., be set to identity.

4 Lid-driven cavity flow

The classical driven cavity flow benchmark, considers a fluid in a square cavity. The left, bottom and right walls exhibit no-slip Dirichlet boundary conditions ($\boldsymbol{u} = 0$), while the top "wall" is moved with a constant speed. A schematic representation of the problem

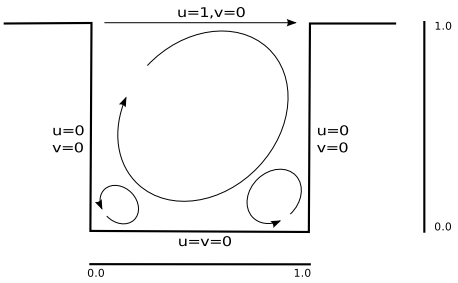

Figure 3: Sketch of lid-driven cavity model.

statement is given in Figure 3. At the upper left and right corners, there is a discontinuity in the velocity boundary conditions producing a singularity in the pressure field at those corners. They can either be considered as part of the upper boundary or as part of the vertical walls. The former case, is referred to as the "leaky" cavity rendering the latter "non-leaky". For equation (15) involves only the gradient of pressure, we fix the pressure solution through a Dirichlet boundary condition of 0 at the lower left corner of the cavity.

Our results, obtained with various B-spline space based discretizations, are compared to reference results from the literature such as those of Ghia [8]. Furthermore, additional comparisons are done with highly accurate, spectral (Chebyshev Collocation) method based solutions of Botella [2] showing convergence up to seven digits.

For an Isogeometric Analysis based approximation of the unknowns in (15), suitable B-spline or NURBS spaces, as defined in Section 2, need to be specified. We use an LBB-stable Taylor-Hood like space pair in the parametric spline domain, where $\hat{Q}_h^{TH} \equiv \hat{Q}_h^{TH}(\mathbf{p}, \boldsymbol{\alpha}) = \mathcal{S}_{\alpha_1,\alpha_2}^{p_1,p_2} \circ \mathbf{F}^{-1}$ and $\hat{\mathbf{V}}_h^{TH} = \boldsymbol{\mathcal{S}}_{\alpha_1,\alpha_2}^{p_1+1,p_2+1} \circ \mathbf{F}^{-1}$, are B-spline spaces for the approximation of pressure and velocity function, respectively [4]. A downcast of the variational formulation (16) to the discrete level, gives rise to the problem statement:

$$\begin{cases} \text{Find } \boldsymbol{v} \in \boldsymbol{\mathcal{H}}_{\Gamma_D}^{1,h}(\Omega) \cap \hat{\mathbf{V}}_h^{TH} \text{ and } p \in \mathcal{L}_2^h(\Omega)/\mathbb{R} \cap \hat{Q}_h^{TH} \text{ such that,} & \\ a(\boldsymbol{w^h}, \boldsymbol{v^h}) + c(\boldsymbol{v^h}; \boldsymbol{w^h}, \boldsymbol{v^h}) + b(\boldsymbol{w^h}, p^h) = (\boldsymbol{w^h}, \boldsymbol{b^h}) + (\boldsymbol{w^h}, \boldsymbol{t^h})_{\Gamma_N} & \forall \boldsymbol{w^h} \in \boldsymbol{\mathcal{H}}_0^{1,h}(\Omega) \cap \hat{\mathbf{V}}_h^{TH} \\ b(\boldsymbol{v^h}, q^h) = 0 & \forall q^h \in \mathcal{L}_2^h(\Omega)/\mathbb{R} \cap \hat{Q}_h^{TH} \end{cases} \tag{29}$$

with superscript h dubbing the mesh family index.

Using the B-spline space pair $\boldsymbol{\mathcal{S}}_{0,0}^{2,2} \times \mathcal{S}_{0,0}^{1,1}$ for the approximation of the velocity and pressure functions, in Figure 4 we present our results for stream function (ψ) and vorticity (ω) profiles for Reynolds numbers $100, 400$ and 1000. Note that we have not taken

any stabilization measures for the advection term. The approach we follow for the com-

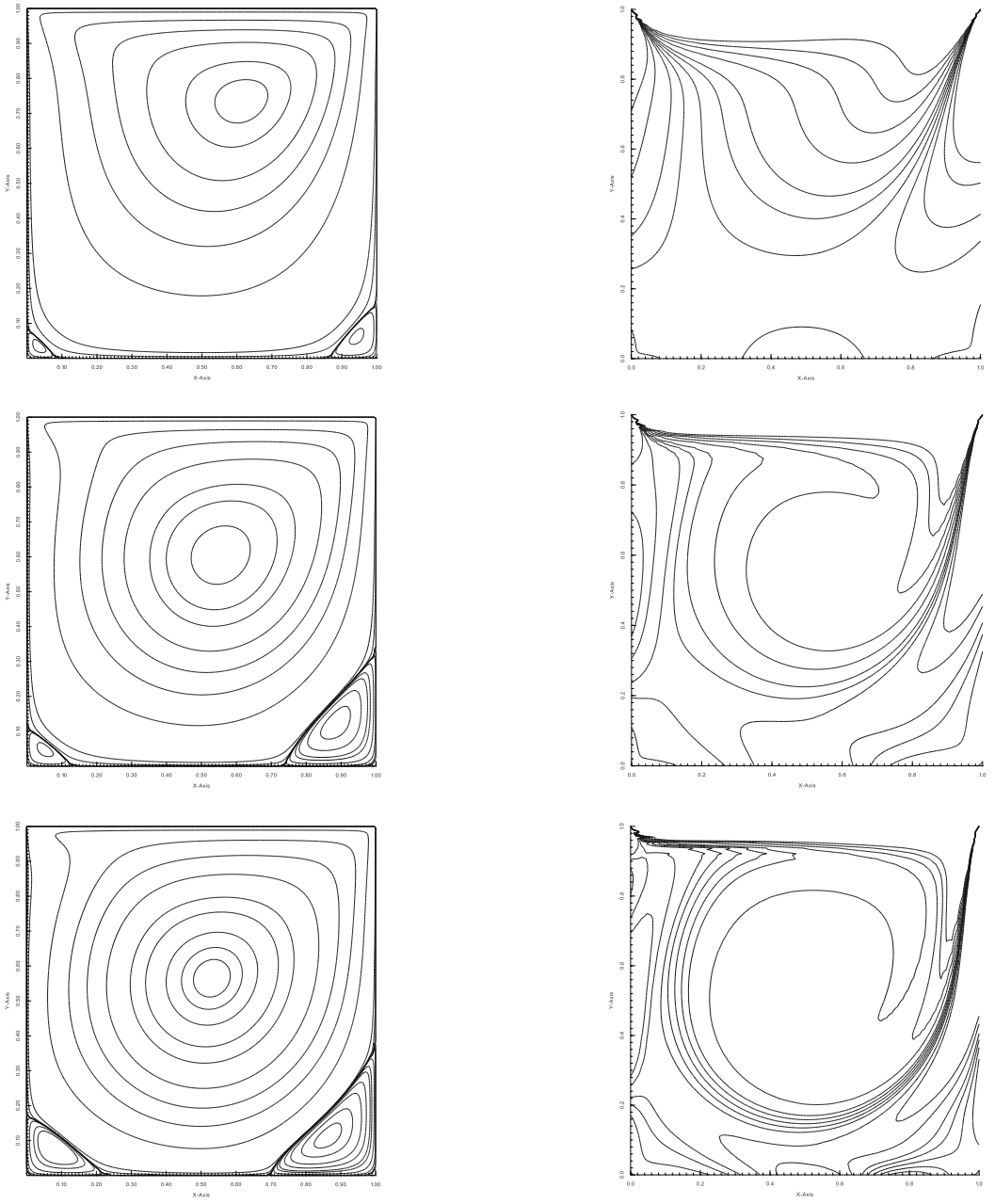

Figure 4: Stream function (left) and vorticity (right) profiles for Reynolds $100, 400$ and 1000 from top to bottom. Respective contour ranges for stream function and vorticity: $\psi_{iso} \in [-10^{-10}, 3 \times 10^{-3}]$, $\omega_{iso} \in [-5, 3]$. Discretization: $\boldsymbol{\mathcal{S}}_{0,0}^{2,2} \times \mathcal{S}_{0,0}^{1,1}$. Refinement level: 6. Number of degrees of freedom: 37507.

putation of the stream function in 2D, is based on solving a Poisson equation for ψ with

the scalar 2D vorticity function on the right hand side:

$$
\begin{aligned}
-\nabla^2\psi &= \omega \\
\omega = \nabla \times \boldsymbol{v} &= \frac{\partial v}{\partial x} - \frac{\partial u}{\partial y}
\end{aligned}
\tag{30}
$$

Equation (30) is easily solvable via FEM/IGA when formulated as a unique boundary value problem on the domain Ω enclosed by the boundary Γ. We set Dirichlet boundary conditions of 0 on the entire boundary when solving for ψ. In Table 1 stream function and vorticity values at the center of the main vortex are presented for Reynolds (Re) numbers $100, 400$ and 1000. We use two different Isogeometric discretizations and compare our results to the reference values of Ghia [8] and Botella [2]. In the latter case, the flow is reversed, that is, the velocity at the upper boundary is $\boldsymbol{u} = (-1, 0)$. However, the flow attributes obtained are mirror-symmetric and comparable to those of older references, such as [8]. Note that the results of [2], utilizing a Chebyshev Collocation method with polynomial degrees as high as 160, are considered highly accurate. For all Reynolds numbers under consideration, our results are in good agreement with the references. Coming up next, we depict our approximations of the u- and v-velocity components along

	Scheme	Grid	x	y	ψ	ω
Re 100	$\boldsymbol{\mathcal{S}}^{2,2}_{0,0} \times \mathcal{S}^{1,1}_{0,0}$	129×129	0.6150	0.7350	-0.1035165	3.15350
	$\boldsymbol{\mathcal{S}}^{6,6}_{4,4} \times \mathcal{S}^{5,5}_{4,4}$	133×133	0.6150	0.7350	-0.1035159	3.15383
	Ghia [8]	129×129	0.6172	0.7344	-0.1034230	3.16646
Re 400	$\boldsymbol{\mathcal{S}}^{2,2}_{0,0} \times \mathcal{S}^{1,1}_{0,0}$	129×129	0.5550	0.6050	-0.113996	2.29470
	$\boldsymbol{\mathcal{S}}^{6,6}_{4,4} \times \mathcal{S}^{5,5}_{4,4}$	133×133	0.5550	0.6050	-0.113988	2.29448
	Ghia [8]	129×129	0.5547	0.6055	-0.113909	2.29469
Re 1000	$\boldsymbol{\mathcal{S}}^{2,2}_{0,0} \times \mathcal{S}^{1,1}_{0,0}$	129×129	0.5300	0.5650	-0.1189511	2.067930
	$\boldsymbol{\mathcal{S}}^{6,6}_{4,4} \times \mathcal{S}^{5,5}_{4,4}$	133×133	0.5300	0.5650	-0.1189341	2.067710
	Botella [2]	N = 48	0.5308	0.5652	-0.1189249	2.067396
	Botella [2]	N = 96	0.5308	0.5652	-0.1189366	2.067750
	Botella [2]	N = 160	0.5308	0.5652	-0.1189366	2.067753
	Ghia [8]	129×129	0.5313	0.5625	-0.1179290	2.049680

Table 1: Location, stream function and vorticity of the primary vortex for Re 100, 400 and 1000. N refers to the degree of the Chebyshev polynomials used by Botella on an N+1×N+1 Gauss-Lobatto grid.

vertical and horizontal lines through the geometric center of the cavity, respectively. The corresponding results, are presented graphically in Figure 5. As for the discretization, we chose a $\mathcal{C}^0$ B-spline space pair $\boldsymbol{\mathcal{S}}^{2,2}_{0,0} \times \mathcal{S}^{1,1}_{0,0}$ spanned over a mesh of 129×129 grid points. Except for one irregularity with respect to the v-velocity component (see Fig. 5) computations in Re 400 case - which may have been caused due to typing issues - the results follow the reference data of [8]. Beside presented results w.r.t the $\boldsymbol{\mathcal{S}}^{2,2}_{0,0} \times \mathcal{S}^{1,1}_{0,0}$ space, we come up with additional ones associated to both an approximation space with higher regularity $\boldsymbol{\mathcal{S}}^{6,6}_{4,4} \times \mathcal{S}^{5,5}_{4,4}$ ($\mathcal{C}^4$) and a reversed flow direction ($\boldsymbol{u} = (-1, 0)$), such as the setup used in [2]. A graphical representation of velocity component and vorticity data approximated in the above described $\mathcal{C}^4$ space, exhibiting excellent agreement with the ones stemming from the reference using a spectral method [2], is illustrated in Figure 6.

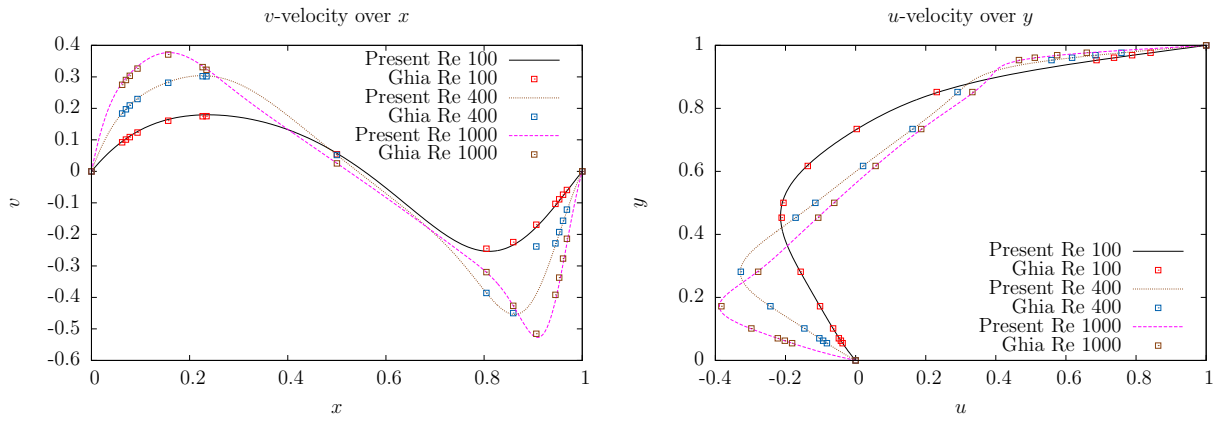

Figure 5: Profiles of v- and u-velocity components over horizontal and vertical lines through geometric center of the cavity for Re $100, 400$ and 1000. Discretization: $\boldsymbol{\mathcal{S}}_{0,0}^{2,2} \times \mathcal{S}_{0,0}^{1,1}$; 129×129 grid points.

4.1 Regularized driven cavity flow

In the regularized lid-driven cavity flow scenario [3], the flow domain is a unit square exhibiting no-slip Dirichlet boundary conditions at the vertical and lower horizontal boundaries. In a standard lid-driven cavity flow setup, the velocity at the top boundary is taken to be constant leading to pressure singularities in the upper left and right domain corners. In order to avoid the singularities, the regularized lid-driven cavity flow problem defines the following velocity profile on the top boundary

$$\mathbf{u}_{lid} = [-16x^2(1-x)^2, 0] \tag{31}$$

Fixing the pressure at the lower left domain node with $p = 0$, we compute the global quantities KINETIC ENERGY (E) and ENSTROPHY (Z)

$$E = \frac{1}{2}\int_\Omega \|\mathbf{u}\|^2 \,\mathrm{d}x, \qquad Z = \frac{1}{2}\int_\Omega \|\omega\|^2 \,\mathrm{d}x, \tag{32}$$

where $\omega = \frac{\partial v}{\partial x} - \frac{\partial u}{\partial y}$ denotes the vorticity.

In Table 2 we compare our results for Reynolds number 1000 to those published in [3] and [13]. All three isogeometric finite element pairs in charge produced very satisfactory results for kinetic energy and enstrophy obviously well integrating with references.

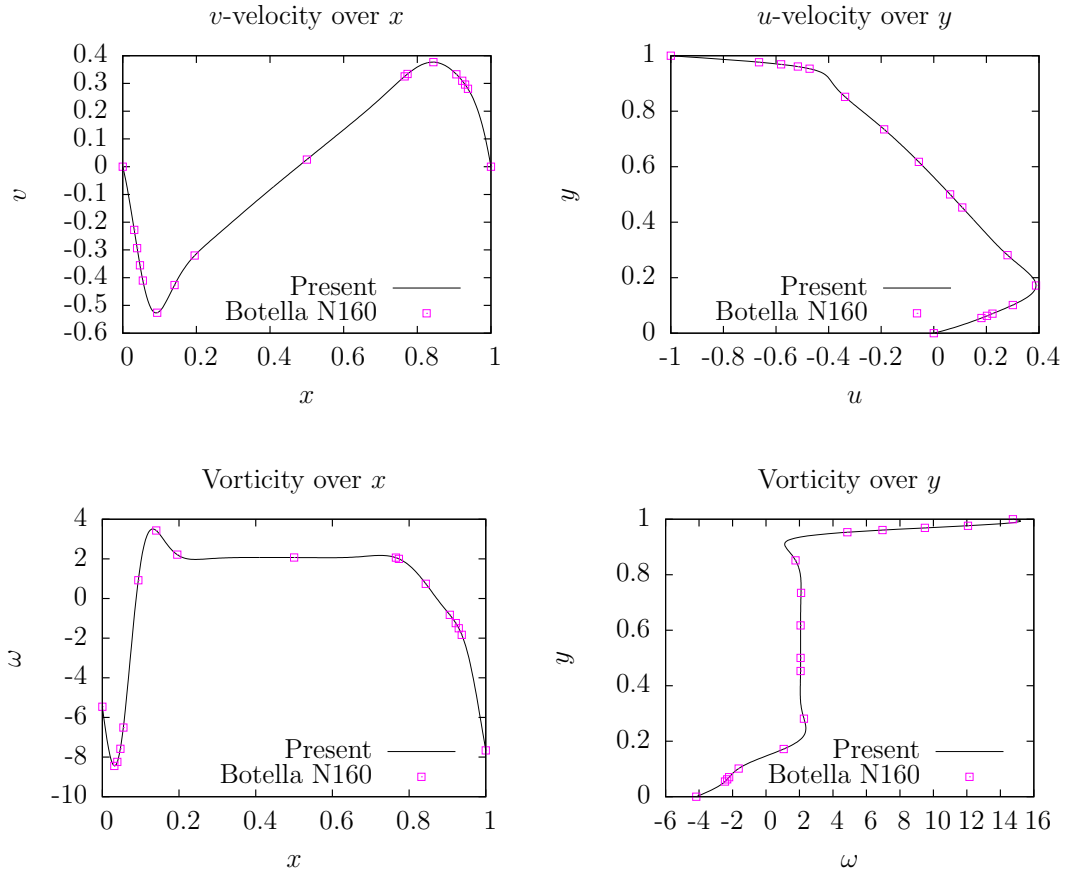

Figure 6: Profiles of v- and u-velocity components and vorticity over horizontal and vertical lines through geometric center of the cavity for Re 1000. Discretization: $\boldsymbol{\mathcal{S}}_{4,4}^{6,6} \times \mathcal{S}_{4,4}^{5,5}$; 133 × 133 grid points.

5 Flow around cylinder

Flow around an obstacle in a channel, is a prominent configuration for the assessment of flow affiliated attributes, produced by a numerical technique in charge with the analysis. Placing our focus on the classical flow around a circular obstacle benchmark, the computational scenario follows the lines of [7, 12, 15] and defines the underlying geometry as a pipe where a circular cylinder of radius $r = 0.05$ has been cut out, that is, $\Omega = [0, 2.2] \times [0, 0.41] \setminus B_r(0.2, 0.2)$. The fluid density and kinematic viscosity are taken as $\rho = 1$ and $\nu = 0.001$. We require no-slip boundary conditions for the lower and upper walls $\Gamma_1 = [0, 2.2] \times \{0\}$ and $\Gamma_3 = [0, 2.2] \times \{0.41\}$ as well as the boundary $S = \partial B_r(0.2, 0.2)$: $u_{|\Gamma_1} = u_{|\Gamma_3} = u_{|S} = 0$. On the left edge $\Gamma_4 = \{0\} \times [0, 0.41]$, a parabolic inflow profile is prescribed, $u(0, y) = \left(\frac{4Uy(0.41-y)}{0.41^2}, 0\right)$, with a maximum velocity $U = 0.3$. On the right edge $\Gamma_4 = \{2.2\} \times [0, 0.41]$, do-nothing boundary conditions define the outflow, $\nu\partial_\eta u - p\eta = 0$ with η denoting the outer normal vector. For a maximum

Scheme	Grid(points)	Kinetic Energy	Enstrophy	Elements	Level
$\boldsymbol{\mathcal{S}}^{2,2}_{0,0} \times \mathcal{S}^{1,1}_{0,0}$	65×65	0.022909	4.80747	32×32	$L5$
	129×129	0.022778	4.82950	64×64	$L6$
	257×257	0.022767	4.83041	128×128	$L7$
	513×513	0.022767	4.83043	256×256	$L8$
$\boldsymbol{\mathcal{S}}^{3,3}_{0,0} \times \mathcal{S}^{2,2}_{0,0}$	49×49	0.022905	4.81717	16×16	$L4$
	97×97	0.022773	4.83079	32×32	$L5$
	193×193	0.022767	4.83047	64×64	$L6$
	385×385	0.022767	4.83042	128×128	$L7$
$\boldsymbol{\mathcal{S}}^{3,3}_{1,1} \times \mathcal{S}^{2,2}_{1,1}$	66×66	0.022777	4.82954	32×32	$L5$
	130×130	0.022767	4.83048	64×64	$L6$
	258×258	0.022767	4.83046	128×128	$L7$
Ref. [3] (Bruneau)	64×64	0.021564	4.6458		
	128×128	0.022315	4.7711		
	256×256	0.022542	4.8123		
	512×512	0.022607	4.8243		
Ref. [13] (Q2P1)	64×64	0.022778	4.82954		
	128×128	0.022768	4.83040		
	256×256	0.022766	4.83050		

Table 2: Kinetic energy and enstrophy of the regularized cavity flow for Reynolds 1000.

velocity of $U = 0.3$, the parabolic profile results in a mean velocity $\bar{U} = \frac{2}{3} \cdot 0.3 = 0.2$. The flow configurations characteristic length is $D = 2 \cdot 0.05 = 0.1$ the diameter of the object perpendicular to the flow direction. This particular problem configuration yields Reynolds number $\mathrm{Re} = \frac{\bar{U}D}{\nu} = \frac{0.2 \cdot 0.1}{0.001} = 20$ for which the flow is considered stationary.

Following the above setup for $\mathrm{Re} = 20$, we present the results of the application of Isogeometric Analysis with a special emphasis on approximated drag and lift values related to the entire obstacle boundary.
With S dubbing the surface of the obstacle, $\boldsymbol{n}_S$ its inward pointing unit normal vector w.r.t. the computational domain Ω, tangent vector $\boldsymbol{\tau} := (n_y, -n_x)^T$ and $\boldsymbol{u}_\tau := \boldsymbol{u} \cdot \boldsymbol{\tau}$, the drag and lift forces are given by

$$\begin{aligned} F_{\text{drag}} = \int_S \left(\rho\nu \frac{\partial \boldsymbol{u}_\tau}{\partial \boldsymbol{n}_S} n_y - p n_x \right) ds, \quad F_{\text{lift}} = -\int_S \left(\rho\nu \frac{\partial \boldsymbol{u}_\tau}{\partial \boldsymbol{n}_S} n_x - p n_y \right) ds \\ C_{\text{drag}} = \frac{2}{\rho \bar{U}^2 D H} F_{\text{drag}}, \quad C_{\text{lift}} = \frac{2}{\rho \bar{U}^2 D H} F_{\text{lift}}, \end{aligned} \tag{33}$$

where $\boldsymbol{u}, p$ and H, represent velocity, pressure and channel height, respectively [11]. We follow, however, the alternative approach of [11, 16] and evaluate a volume integral for the approximations of the drag and lift coefficients. Given filter functions

$$\boldsymbol{v}_{d|S} = (1,0)^T, \boldsymbol{v}_{d|\bar{\Omega}-S} = \boldsymbol{0} \qquad \boldsymbol{v}_{l|S} = (0,1)^T, \boldsymbol{v}_{l|\bar{\Omega}-S} = \boldsymbol{0}, \tag{34}$$

the corresponding volume integral expressions read

$$\begin{aligned} C_{\text{drag}} &= -\frac{2}{\rho \bar{U}^2 D H} \left[(\nu \nabla \boldsymbol{u}, \nabla \boldsymbol{v_d}) - (p, \nabla \cdot \boldsymbol{v_d}) \right] \\ C_{\text{lift}} &= -\frac{2}{\rho \bar{U}^2 D H} \left[(\nu \nabla \boldsymbol{u}, \nabla \boldsymbol{v_l}) - (p, \nabla \cdot \boldsymbol{v_l}) \right] \end{aligned} \tag{35}$$

with $(\cdot,\cdot)$ denoting the $L^2(\Omega)$ inner product.

We model the computational domain as a multi-patch NURBS mesh (see Fig. 7), since the parametric space of a multi-variate NURBS patch exhibits a tensor product structure, and thus, is not mappable to any other topology than a cube in the respective N-dimensional space. However, the multi-patch setup yields a perfect mathematical representation of the circular boundary and in particular avoids its approximation with straight line segments. Note that each quarter of the "obstacle circle" can be modeled exactly with a NURBS curve of degree 2 and just 3 control points. Since the ability to exactly represent conical sections is restricted to rational B-splines only, a NURBS mesh came in handy for modeling of the computational domain. With the degrees of

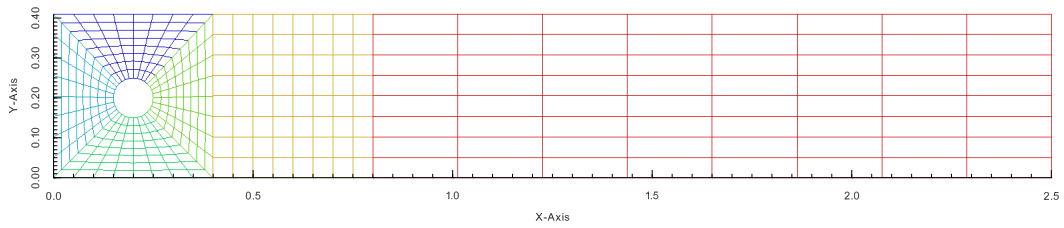

Figure 7: Multi-patch NURBS domain for flow around cylinder. Each uniquely colored initial 1×1 element patch has been refined three times, giving rise to 8×8 elements in each patch, eventually.

freedom being defined on the NURBS control points, and the latter failing to have a straightforward and obvious association to a distinct position on the physical mesh, the question arises how to set up the inflow boundary condition on the control points to finally obtain a parabolic inflow profile. We performed a finite element L^2-projection

$$\int_\Omega (f - P_h f)\, w \,\mathrm{d}\Omega = 0, \quad \forall w \in \mathcal{W}_h \tag{36}$$

of the inflow profile f on the control points associated with the left boundary in Fig. 7, whereby $\mathcal{W}_h$ denotes a suitable discrete space of weighting/test functions.

Our results for drag, lift and pressure drop, evidently showing good agreement with the reference, are depicted alongside reference values in Table 3.

Comparing the presented $\mathcal{C}^0$ and $\mathcal{C}^1$ IGA based discretizations, one observes in the latter case a reduced amount of degrees of freedom on the same number of elements, which is due to the extended support of the respective basis functions. This leads on mesh refinement levels ≥ 1 to numbers of degrees of freedom which are not well comparable between the two IGA based discretizations. However, a linear interpolation of the drag and lift coefficients, as depicted in Figure 8, delineates the accuracy wise superiority of the high continuity $\mathcal{C}^1$ approach. The semantics of superiority is in terms of gained accuracy with respect to the number of degrees of freedom invested. However, for the sake of a fair evaluation, we point out that approximation in high degree and regularity

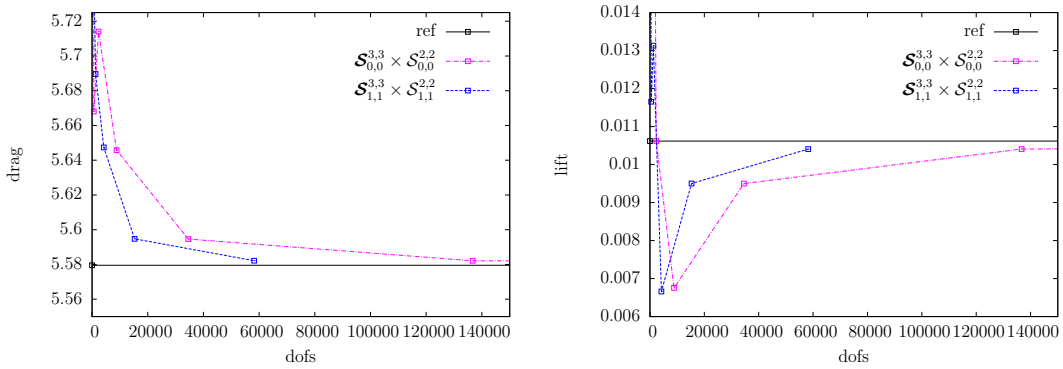

Figure 8: Drag and lift approximation results compared to reference [7]. Discretizations: $\boldsymbol{\mathcal{S}}^{3,3}_{0,0} \times \mathcal{S}^{2,2}_{0,0}$; $\boldsymbol{\mathcal{S}}^{3,3}_{1,1} \times \mathcal{S}^{2,2}_{1,1}$

spaces, comes at a cost of more expensive cubature rules reflecting the basis function degrees (#cub.pts. $= p + 1$), and the evaluation of high degree, thus more expensive, spline basis functions. Moreover, as the supports of the basis functions extend with rising regularities, so do the couplings among the degrees of freedom. This contributes to a greater matrix fill-in and may increase the burden on the shoulders of existing solution methods for sparse linear system of equations.

It should be noted that the solutions we obtained with the $\mathcal{C}^{>0}$ approaches still reduce to $\mathcal{C}^0$ at patch boundaries. There exist means to overcome this deficiency [5], none of them have been considered in this study, though.

Scheme	C_{drag}	C_{lift}	Δp	Degrees of freedom	Elements	Level
$\boldsymbol{\mathcal{S}}^{3,3}_{0,0} \times \mathcal{S}^{2,2}_{0,0}$	6.87638	0.102597	0.206858	180	6	$L0$
$\boldsymbol{\mathcal{S}}^{3,3}_{0,0} \times \mathcal{S}^{2,2}_{0,0}$	5.66806	0.031363	0.118502	624	24	$L1$
$\boldsymbol{\mathcal{S}}^{3,3}_{0,0} \times \mathcal{S}^{2,2}_{0,0}$	5.71406	0.010623	0.116011	2304	96	$L2$
$\boldsymbol{\mathcal{S}}^{3,3}_{0,0} \times \mathcal{S}^{2,2}_{0,0}$	5.64576	0.006755	0.116750	8832	384	$L3$
$\boldsymbol{\mathcal{S}}^{3,3}_{0,0} \times \mathcal{S}^{2,2}_{0,0}$	5.59464	0.009499	0.117328	34560	1536	$L4$
$\boldsymbol{\mathcal{S}}^{3,3}_{0,0} \times \mathcal{S}^{2,2}_{0,0}$	5.58212	0.010407	0.117490	136704	6144	$L5$
$\boldsymbol{\mathcal{S}}^{3,3}_{0,0} \times \mathcal{S}^{2,2}_{0,0}$	5.57992	0.010586	0.117516	543744	24576	$L6$
$\boldsymbol{\mathcal{S}}^{3,3}_{1,1} \times \mathcal{S}^{2,2}_{1,1}$	6.87638	0.102597	0.206858	180	6	$L0$
$\boldsymbol{\mathcal{S}}^{3,3}_{1,1} \times \mathcal{S}^{2,2}_{1,1}$	5.76865	0.011653	0.112236	432	24	$L1$
$\boldsymbol{\mathcal{S}}^{3,3}_{1,1} \times \mathcal{S}^{2,2}_{1,1}$	5.68962	0.013130	0.115025	1260	96	$L2$
$\boldsymbol{\mathcal{S}}^{3,3}_{1,1} \times \mathcal{S}^{2,2}_{1,1}$	5.64735	0.006661	0.116317	4212	384	$L3$
$\boldsymbol{\mathcal{S}}^{3,3}_{1,1} \times \mathcal{S}^{2,2}_{1,1}$	5.59476	0.009502	0.117224	15300	1536	$L4$
$\boldsymbol{\mathcal{S}}^{3,3}_{1,1} \times \mathcal{S}^{2,2}_{1,1}$	5.58215	0.010408	0.117489	58212	6144	$L5$
Ref. [7, 12]	5.57953523384	0.010618948146	0.11752016697			

Table 3: Approximation results for drag, lift and pressure drop (Δp).

In the following we turn our attention to the TIME PERIODIC DFG FLOW AROUND CYLINDER BENCHMARK FOR RE 100, as described in [6, 15]. Here the maximum velocity of the parabolic inflow profile amounts to $U = 1.5$, yielding $\text{Re} = \frac{\bar{U}D}{\nu} = \frac{\frac{2}{3}\cdot\frac{3}{2}\cdot 0.1}{0.001} = 100$. In order to obtain a time profile for the drag and lift quantities, Isogeometric Analysis was

applied on the unsteady incompressible Navier-Stokes equations (18) using the B-spline spaces $\hat{Q}_h^{TH} = \mathcal{S}_{0,0}^{2,2} \circ \mathbf{F}^{-1}$ and $\hat{\mathbf{V}}_h^{TH} = \boldsymbol{\mathcal{S}}_{0,0}^{3,3} \circ \mathbf{F}^{-1}$ for pressure and velocity, respectively. This corresponds to solving the system in a fully coupled manner since we solve for all unknown functions simultaneously.

The semi-discretized counterpart of the variational formulation (19) reads:

$$\begin{cases} \text{Find } \boldsymbol{v} \in \boldsymbol{\mathcal{H}}_{\Gamma_D}^{1,h}(\Omega) \cap \hat{\mathbf{V}}_h^{TH} \times]0,T[\text{ and } p \in \mathcal{L}_2^h(\Omega)/\mathbb{R} \cap \hat{Q}_h^{TH} \times]0,T[\text{ such that,} \\ \forall \boldsymbol{w}^h \in \boldsymbol{\mathcal{H}}_0^{1,h}(\Omega) \cap \hat{\mathbf{V}}_h^{TH} \text{ and } \forall q^h \in \mathcal{L}_2^h(\Omega)/\mathbb{R} \cap \hat{Q}_h^{TH} \\ (\boldsymbol{w}^h, \boldsymbol{v}_t^h) + a(\boldsymbol{w}^h, \boldsymbol{v}^h) + c(\boldsymbol{v}^h; \boldsymbol{w}^h, \boldsymbol{v}^h) + b(\boldsymbol{w}^h, p^h) = \ (\boldsymbol{w}^h, \boldsymbol{b}^h) + (\boldsymbol{w}^h, \boldsymbol{t}^h)_{\Gamma_N} \\ b(\boldsymbol{v}^h, q^h) = 0 \end{cases} \tag{37}$$

For the time discretization, the single step θ-scheme with $\theta = 0.5$ is used, leading to the 2-nd order accurate implicit Crank-Nicolson scheme [17]. Together with the space discretization the following nonlinear block system has to be solved in every time step.

$$\begin{pmatrix} \frac{1}{\Delta t}\mathbf{M} + \theta(\mathbf{D} + \mathbf{C}(v^{n+1})) & \mathbf{G} \\ \mathbf{G}^T & \mathbf{0} \end{pmatrix} \begin{pmatrix} \mathbf{v}^{n+1} \\ \mathbf{p}^{n+1} \end{pmatrix} = \begin{pmatrix} \frac{1}{\Delta t}\mathbf{M} - (1-\theta)(\mathbf{D} + \mathbf{C}(v^n)) & \mathbf{0} \\ \mathbf{0} & \mathbf{0} \end{pmatrix} \begin{pmatrix} \mathbf{v}^n \\ \mathbf{p}^n \end{pmatrix} + \theta \mathbf{f}^{n+1} + (1-\theta)\mathbf{f}^n \tag{38}$$

In the above system, $\mathbf{M}, \mathbf{D}, \mathbf{C}, \mathbf{G}$ and $\mathbf{G^T}$ denote the mass, diffusion, advection, gradient and divergence matrices, respectively. The body forces are discretized into $\mathbf{f}$.
An exemplary sectional view of the approximated lift time profile is presented in Figure 9. Our results are plotted alongside those obtained from [6] using Q_2/P_1^{disc} finite elements (without stabilization) for space discretization and Crank-Nicolson scheme for time discretization. All computations performed, are based on the NURBS mesh depicted in Figure 7. Note that it substantially differs from that used in [6] in terms of structure and number of degrees of freedom. In fact, our mesh has roughly 18% less degrees of freedom on each level as can be seen from Table 4. For all mesh levels we

Level	#DOFs NURBS mesh (7)	#DOFs reference mesh ([6])	Ratio
L3	8832	10608	$\sim 8/10$
L4	34560	42016	$\sim 8/10$
L5	136704	167232	$\sim 8/10$

Table 4: Comparison of the number of degrees of freedom per level

performed an intermediate computation with a very coarse time step ($\Delta t = 1/10$) for a total time of 35 simulation seconds. This yielded a profile which we took as initial solution for the final computation with a finer time step, scheduled for 30 simulation seconds. Note that the depicted time interval is chosen arbitrarily after the drag and lift profiles were considered developed. In addition, the curves have been shifted in time in order to facilitate comparison. As far as the treatment of nonlinearity is concerned, for every time step, the nonlinear iteration loop was iterated until the nonlinear residual of equation (38) was reduced to 10^{-3} of its initial value. Tables 5 and 6 supply minimum, maximum, mean and amplitude values for the drag and lift coefficients w.r.t different mesh levels. In addition to min/max drag and lift coefficients, further quantities of

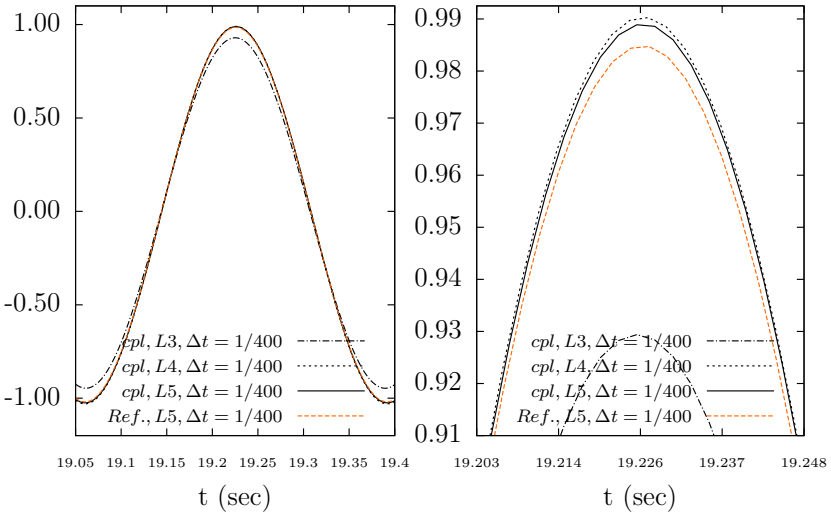

Figure 9: Sectional views of lift time profile.

Level	Δt	min(C_{drag})	max(C_{drag})	mean(C_{drag})	amp(C_{drag})
L3	1/400	3.2732	3.3329	3.3031	5.966E-2
L4	1/400	3.2218	3.2857	3.2537	6.394E-2
L5	1/400	3.1757	3.2392	3.2075	6.354E-2

Table 5: min/max drag coefficient values

Level	Δt	min(C_{lift})	max(C_{lift})	mean(C_{lift})	amp(C_{lift})
L3	1/400	-0.9466	0.92939	-0.00861	1.8760
L4	1/400	-1.0302	0.99033	-0.01995	2.0206
L5	1/400	-1.0249	0.98903	-0.01794	2.0139

Table 6: min/max lift coefficient values

interest are the lift profile frequency (f) and Strouhal number ($\text{St} = \frac{Df}{U}$) which we provide values for in Table 7. Bearing in mind the significantly smaller number of degrees of

Level	Δt	$1/f$ (present)	St (present)	$1/f$ [6]	St [6]
L3	1/400	3.2804E-1	0.30484	3.3000E-01	0.30303
L4	1/400	3.3154E-1	0.30162	3.3250E-01	0.30075
L5	1/400	3.3143E-1	0.30172	3.3000E-01	0.30303

Table 7: Frequency and Strouhal numbers for different mesh levels.

freedom invested ($\sim 18\%$ less) for the approximation of the physical quantities of interest and observing a satisfying agreement with results obtained from the alternative numerical implementation of [6] using Q_2/P_1^{disc} finite elements, the overall conclusions drawn, depict Isogeometric Analysis as a robust and powerful tool at hand well applicable to problems considered in this study.

6 Summary and conclusions

Isogeometric Analysis was applied to well known model flow problems in order to investigate its approximation properties and numerical behavior. Starting off with the lid-driven cavity flow problem, including its regularized version, we have shown in Chapter 4 that the approximated flow attributes are very well comparable with reference results partially obtained with a highly accurate, spectral (Chebyshev Collocation) method [2]. Moreover, in Chapter 4.1 we have extended our view to global quantities such as kinetic energy and enstrophy and have provided results which are at least as good as reference results obtained with other approaches such as Q_2P_1 standard finite elements [13] and a high order finite difference scheme utilized in [3].

In addition to cavity flow, we chose the prominent flow around cylinder benchmark, proposed in [15], to explore the approximation traits of isogeometric finite elements. The usage of a $\mathcal{C}^1$ B-spline element pair, turned out to be superior to its $\mathcal{C}^0$ counterpart in terms of the number of degrees of freedom required to gain a certain accuracy. This comes, however, at a cost of more expensive evaluations of higher degree B-spline/NURBS basis functions and increased degree of freedom coupling, leading to broader matrix stencils. Thus, care must be taken with claims regarding general superiority of higher continuity ($\mathcal{C}^{\geq 1}$) approximations.

We eventually turned our attention to the unsteady Re-100 flow around cylinder case involving the transient form of the Navier-Stokes equations. The governing equations were discretized in time with a second order implicit time discretization scheme and finally solved in a fully coupled mode. Given the fact that the multi-patch NURBS mesh we used (see Fig. 7) is shown to have about 1/5 less degrees of freedom than the reference mesh used in [6, 7, 15], the presented time profiles of the physical quantities drag and lift are satisfactorily.

Isogeometric Analysis proved for us to be a solid and reliable technology showcasing unique features. For Taylor-Hood like B-spline elements we carried our analysis upon, it turned out to be just a matter of changing settings in a configuration file to set up a desired B-spline element of a specific degree and continuity. This is without any doubt a huge benefit when compared to usual finite elements where one needs to provide an implementation for each element type. Moreover, for B-spline/NURBS geometries, already exactly representing a computational domain on the coarsest level, the process of meshing is entirely pointless. The mathematical definition of a B-spline/NURBS already defines a tensor product mesh eligible to NURBS based refinement techniques such as h-, p- or k-refinement [5, 14].
However, on a final note, the true virtue of the technology can be better exploited in applications involving high order partial differential equations such as e.g. the third order Navier-Stokes-Korteweg [10] or fourth order Cahn-Hilliard equations [9] in combination with complex geometries.

References

[1] Y. Bazilevs, L. Beirao da Veiga, J.A. Cottrell, T.J.R. Hughes, and G. Sangalli. Isogeometric analysis: Approximation, stability and error estimates for h-refined meshes. *Math. Models Methods Appl. Sci. 16, 1031*, 2006.

[2] O. Botella and R. Peyret. Benchmark spectral results on the lid-driven cavity flow. *Computers & Fluids*, Volume 27, Issue 4:421–433, 1 May 1998.

[3] Charles-Henri Bruneau and Mazen Saad. The 2d lid-driven cavity problem revisited. *Computers & Fluids*, 35, Issue 3:326–348, March 2006.

[4] A. Buffa, C. de Falco, and G. Sangalli. Isogeometric analysis: Stable elements for the 2D Stokes equation. *International Journal for Numerical Methods in Fluids. Special Issue: Numerical Methods for Multi-material Fluids and structures, MULTIMAT-2009*, 65 Issue 11-12:1407–1422, 20 - 30 April 2011.

[5] J. Austin Cottrell, Thomas J. R. Hughes, and Yuri Bazilevs. *Isogeometric Analysis: Toward Integration of CAD and FEA*. Wiley; 1 edition (September 15, 2009), 2009.

[6] `http://www.featflow.de/en/benchmarks/cfdbenchmarking/flow/dfg_benchmark2_re100.html` [Online; accessed 01-Oct-2014].

[7] `http://www.featflow.de/en/benchmarks/cfdbenchmarking/flow/dfg_benchmark_re20.html` [Online; accessed 01-Oct-2014].

[8] U. Ghia, K. N. Ghia, and C.T. Shin. High-Re solutions for incompressible flow using the Navier-stokes Equations and a multigrid method. *Journal of computational physics*, 48, Issue 3:387–411, December 1982.

[9] Hector Gomez, Victor M. Calo, Yuri Bazilevs, and Thomas J.R. Hughes. Isogeometric analysis of the Cahn-Hilliard phase-field model. *Computer Methods in Applied Mechanics and Engineering.*, 197, Issues 49–50:4333–4352, 15 September 2008.

[10] Hector Gomez, Thomas J.R. Hughes, Xesus Nogueira, and Victor M. Calo. Isogeometric analysis of the isothermal Navier-Stokes-Korteweg equations. *Computer Methods in Applied Mechanics and Engineering*, 199, Issues 25–28:1828–1840, 15 May 2010.

[11] Volker John. Higher order finite element methods and multigrid solvers in a benchmark problem for the 3D Navier–Stokes equations. *International Journal for Numerical Methods in Fluids*, 40, Issue 6:775–798, 2002.

[12] G. Nabh. *On High Order Methods for the Stationary Incompressible Navier-Stokes Equations*. PhD thesis, University of Heidelberg, 1998.

[13] Masoud Nickaeen, Abderrahim Ouazzi, and Stefan Turek. Newton multigrid least-squares FEM for the V-V-P formulation of the Navier-Stokes equations. *Journal of Computational Physics*, 256:416–427, 1 January 2014.

[14] Les A. Piegl and Wayne Tiller. *The NURBS book*. Monographs in visual communication. Springer, 1995.

[15] M. Schäfer, S. Turek, F. Durst, E. Krause, and R. Rannacher. Benchmark computations of laminar flow around a cylinder, January 1996.

[16] S. Turek, A. Ouazzi, and J. Hron. On pressure separation algorithms (pSepA) for improving the accuracy of incompressible flow simulations. *International Journal for Numerical Methods in Fluids*, 59, Issue 4:387–403, 2009.

[17] Stefan Turek. *Efficient Solvers for Incompressible Flow Problems - An Algorithmic and Computational Approach*, volume 6 of *Lecture Notes in Computational Science and Engineering*. Springer, 1999.